


 Cite this: *Nanoscale*, 2020, **12**, 9462

In situ growth of well-aligned Ni-MOF nanosheets on nickel foam for enhanced photocatalytic degradation of typical volatile organic compounds†

 Xin Ding,^{‡a} Hongli Liu,^{‡a,b} Jiangyao Chen,^{id a,b} Meicheng Wen,^a Guiying Li,^{id a,b} Taicheng An^{id *a} and Huijun Zhao^{id *c}

Exploitation of highly efficient catalysts for photocatalytic degradation of volatile organic compounds (VOCs) under visible light irradiation is highly desirable yet challenging. Herein, well-aligned 2D Ni-MOF nanosheet arrays vertically grown on porous nickel foam (Ni-MOF/NF) without lateral stacking were successfully prepared *via* a facile *in situ* solvothermal strategy. In this process, Ni foam could serve as both a skeleton to vertically support the Ni-MOF nanosheets and a self-sacrificial template to afford Ni ions for MOF growth. The Ni-MOF/NF nanosheet arrays with highly exposed active sites and light harvesting centres as well as fast mass and e⁻ transport channels exhibited excellent photocatalytic oxidation activity and mineralization efficiency to typical VOCs emitted from the paint spray industry, which was almost impossible for their three-dimensional (3D) bulk Ni-MOF counterparts. A mineralization efficiency of 86.6% could be achieved at 98.1% of ethyl acetate removal. The related degradation mechanism and possible reaction pathways were also attempted based on the electron paramagnetic resonance (EPR) and online Time-of-Flight Mass Spectrometer (PTR-ToF-MS) results.

Received 6th February 2020

Accepted 8th April 2020

DOI: 10.1039/d0nr01027h

rsc.li/nanoscale

1. Introduction

Volatile organic compounds (VOCs), mainly emitted from solvent use, paint, petrochemical processing, vehicle exhaust, and many other industrial activities, are becoming a major class of air pollutants.¹ They not only accelerate the formation of secondary organic aerosols and photochemical smog, but also could cause headaches, cancer, mutagenesis and teratogenesis even at very low concentrations.^{2–4} Due to the serious hazard of VOCs to both environment and public health, tremendous efforts have been devoted to developing effective strategies to remove VOCs from polluted air with a minimal environmental impact.^{1,5–10} Among them, semi-

conductor photocatalytic oxidation has been considered as one of the most promising methods for the removal of VOCs,^{7–10} because it holds great promise for mineralizing various VOCs into innocuous constituents under mild conditions and solar light illumination without any other energy input.

The photocatalytic oxidation essentially depends on two key steps: semiconductor catalysts are excited by harvested photons under light irradiation to generate electron-hole pairs (e⁻-h⁺) and they subsequently migrate to the adsorbed molecules like H₂O, O₂, and OH⁻ on the surface of photocatalysts to form reactive species (such as [•]O²⁻ and [•]OH) for degradation of the captured VOCs. Unfortunately, conventional semiconductor catalysts, as the core of this technology, still suffer from insufficient photocatalytic activity, a narrow light response range and poor stability due to their inherent structural characteristics, including a high e⁻-h⁺ recombination rate and low surface area,^{7–10} which greatly impede their practical application under visible light or natural solar light irradiation. Particularly for low concentration VOCs, the limited capture capacity of VOCs onto the catalyst surface makes it more challenging to obtain a tolerable reactivity, usually accompanied by more toxic incomplete oxidation products.¹⁰ Therefore, the exploration of new types of photocatalysts to obtain an optimized photocatalytic performance is rather imperative.

^aGuangdong Key Laboratory of Environmental Catalysis and Health Risk Control, Guangzhou Key Laboratory Environmental Catalysis and Pollution Control, School of Environmental Science and Engineering, Institute of Environmental Health and Pollution Control, Guangdong University of Technology, Guangzhou 510006, China. E-mail: antc99@gdut.edu.cn

^bSynergy Innovation Institute of GDUT, Shantou 515041, China

^cCentre for Clean Environment and Energy, and Griffith School of Environment, Gold Coast Campus, Griffith University, Queensland, 4222, Australia. E-mail: h.zhao@griffith.edu.au

†Electronic supplementary information (ESI) available. See DOI: 10.1039/d0nr01027h

‡Both authors contributed equally to this work and are considered to be co-first authors.

Metal–organic frameworks (MOFs), a particular family of porous materials built from organic linkers with metal ions or clusters,^{11–14} might offer new opportunities for highly efficient photocatalytic degradation of VOCs. Benefitting from their large surface area, ordered pore structure and ultrahigh porosity, MOFs exhibited remarkably high VOC adsorption capacities over traditional porous materials.^{14–16} Additionally, MOF-based photocatalysts have been exploited and successfully applied to liquid phase photocatalysis including CO₂ reduction, water splitting, pollutant degradation, and organic transformations.^{17–21} Notably, it has been suggested that the organic linkers in MOFs could work as light harvesting centres, and the metal cluster nodes could act as inorganic semiconductor dots isolated by the organic linkers and the pores of the MOFs upon photoexcitation, thus making MOFs promising toward photocatalysis. Given the outstanding VOC capture capacity and the high density of semiconductor dots within MOF nodes, the photogenerated holes should be consumed immediately by VOC molecules before the carrier recombination due to plenty of captured reactants around the highly exposed active sites, and thus a high photocatalytic activity would be anticipated for MOF materials. However, MOFs or MOF-based composites to date have been rarely utilized in photocatalytic VOC oxidation.^{22–25} Additionally, the reported three-dimensional (3D) bulk MOF systems of sub-micrometer or micrometer size would cause limited exposure of optical absorption and photocatalytic active centers as well as a long mass/electron transfer distance. In this regard, two-dimensional (2D) MOF nanosheets in nanometer thicknesses with less geometric constraints allow superior electron transfer, fast mass transport and highly exposed active sites compared with their 3D counterparts,^{26–30} which would be expected to maximize their photocatalytic performance. Particularly, the growth of MOF nanosheets on a 3D substrate with spatial orientation could also avoid stacking between MOF nanosheets to improve gas permeation and light penetration, which is also convenient for their practical application in VOC purification.

With the above in mind, we reported well-aligned 2D Ni-MOF nanosheets vertically supported on a porous nickel foam (Ni-MOF/NF) substrate for enhancing the photocatalytic degradation of VOCs for the first time. This material was synthesized by direct *in situ* growth of Ni-MOF on Ni foam without an extra added nickel source, in which Ni foam could be slowly oxidized with the assistance of air and water as well as release Ni²⁺ for Ni-MOF growth. Unexpectedly, the obtained well-aligned Ni-MOF/NF arrays exhibited excellent photocatalytic activity and mineralization efficiency in the photocatalytic oxidation of typical VOCs emitted from the paint spray industry. Mechanistic investigations implied that the unique structure of Ni-MOF/NF, consisting of well-aligned Ni-MOF nanosheet arrays and conductive macroporous Ni foam, was beneficial for improving light harvesting, the accessibility of active sites and fast mass and e⁻ transport, thus forming abundant strong oxidative ·O²⁻ and ·OH radicals and photo-generated h⁺ to decompose the captured VOCs.

2. Experimental section

2.1. Chemicals

Ni foam with a thickness of approximately 1.5 mm was purchased from Changsha Keliyuan Co., Ltd. 2-Methylimidazole (98%), nickel chloride (NiCl₂·6H₂O, A.R.) and sodium formate (≥99.5%) were purchased from Aladdin. 5,5-Dimethyl-1-pyrroline *N*-oxide (DMPO) was purchased from Sigma-Aldrich. Methanol, ethyl acetate, toluene and *n*-butanol were analytical grade, obtained from the Guangzhou Chemical Reagent Factory and used without further purification.

2.2. Materials synthesis

Synthesis of Ni-MOF/NF. Firstly, the Ni foam with a size of 2 cm × 3 cm was successively immersed in an ultrasonic bath of methanol, 1 M HCl and deionized water for 30 min to remove the potential impurities on the surface of Ni foam and then dried under vacuum conditions to achieve activated Ni foam. Afterward, 2-methylimidazole (0.02463 g) and sodium formate (0.0204 g) were dissolved in methanol (20 mL) in a 100 mL Teflon liner by ultrasonication. Then, a piece of activated Ni foam was quickly placed in the above mixed solution. The liner was sealed and heated at 120 °C for 24 h. Briefly, a piece of Ni foam was immersed in a methanol solution of 2-methylimidazole and sodium formate, and then retained at 120 °C for 24 h. After cooling to room temperature, Ni-MOF/NF was washed thoroughly with methanol and deionized water in turn, and dried under vacuum conditions at 80 °C for 12 h.

Synthesis of Ni-MOF. The Ni-MOF was prepared under the same synthesis conditions as Ni-MOF/NF, except for replacing Ni foam with NiCl₂·6H₂O. Typically, NiCl₂·6H₂O (0.0713 g), 2-methylimidazole (0.02463 g), and sodium formate (0.0204 g) were dissolved in methanol (20 mL) in a 100 mL Teflon liner. The mixture was subjected to ultrasonication for 0.5 h, and then heated at 120 °C for 24 h. Subsequently, the generated solid was collected by centrifugation, and washed thoroughly with methanol and deionized water in turn. The as-obtained powder was finally dried under vacuum conditions at 80 °C for 12 h to obtain the activated Ni-MOF.

2.3. Characterization

The morphology of the prepared samples was observed using a Zeiss Merlin instrument with energy dispersive X-ray spectroscopy. Fourier transform infrared spectra were recorded on a Thermo Scientific Nicolet iS10 spectrometer. Nitrogen adsorption–desorption isotherms were obtained at 77 K on a Micromeritics ASAP2460. Prior to analysis, the samples were evacuated at 150 °C for 6 h. UV-Vis diffuse reflectance spectra were recorded with an Agilent Carry 300 spectrophotometer using BaSO₄ as a standard reference in the wavelength range of 200–800 nm. Thermal stabilities of the samples were investigated using a Mettler Toledo thermal gravimetric analyser in a nitrogen atmosphere with a cooling/heating rate of 5 °C min⁻¹.

2.4. Photoelectrochemical measurements

Photoelectrochemical tests were carried out using a standard three-electrode system (Chenhua CHI 600E) with Ag/AgCl as

the reference electrode, and Pt foil as the counter electrode. The bare Ni foam and Ni-MOF/NF were directly used for the working electrode. The used electrolyte was 0.5 M Na₂SO₄ aqueous solution. A 300 W Xe lamp with an irradiance intensity of 303 mW cm⁻² was chosen as the light source, and its output light spectrum is shown in Fig. S1.† For the powder Ni-MOF material, 6 mg of activated Ni-MOF were dispersed in a mixture of 20 μL of naphthol, 0.75 mL of ethanol and 0.25 mL of deionized water by ultrasonication for 20 min. Subsequently, the powder Ni-MOF working electrode was obtained by coating the above suspension onto the conductive side of the FTO glass substrate and finally dried to remove residuals.

The photocurrents of the samples were measured by a constant voltage amperometric method under intermittent irradiation with 0.8 V chopped light and a linear sweep voltammetry (LSV) curve was obtained with a voltage from 1.0 to 1.5 V. Electrochemical impedance spectroscopy (EIS) was performed in the frequency ranging from 0.01 to 10⁵ Hz with a bias potential of 1.0 V. Mott-Schottky plots for Ni-MOF/NF and Ni-MOF were both recorded at frequencies of 500 and 1000 Hz, respectively.

2.5. Photocatalytic degradation and intermediate identification experiments

Direct photocatalytic oxidation of typical VOCs. The photocatalytic performance of the samples was measured by degrading typical VOCs emitted from the paint spray industry in a fixed-bed quartz reactor (Fig. S2†) with a continuous flow mode under atmospheric pressure. A 300 W Xenon lamp with an irradiance intensity of 303 mW cm⁻² (Fig. S1†) was used as the light source, which was fixed vertically at the top of the reactor with a distance of 10 cm. The temperature of the reactor was regulated at 30 ± 0.5 °C using a digital temperature controller. After loading the material into the reactor, VOC gas with a concentration of 70 ± 1 ppmv balanced by air was steadily introduced into the reactor at a flow rate of 35 mL min⁻¹. Meanwhile, the lamp was immediately turned on when starting the photocatalytic reaction. The concentrations of VOCs and the formed CO₂ during the photocatalytic degradation process were monitored using an online gas chromatograph equipped with two flame ionization detectors (FID). One FID was used for removal efficiency determination, and another one was used for mineralization efficiency determination of VOCs. At each given time interval, 1 mL of the effluent gas was injected into the gas chromatograph.

The removal efficiency of VOCs was evaluated based on the following equation:

$$\text{Removal efficiency of VOC} = \frac{C_0 - C_t}{C_0} \times 100\%$$

$$\text{Mineralization efficiency of VOC} = \frac{C_{t\text{CO}_2}}{N \times C_0} \times 100\%$$

$$\text{CO}_2 \text{ selectivity} = \frac{C_{t\text{CO}_2}}{N \times (C_0 - C_t)} \times 100\%$$

where C_0 is the initial concentration of VOC ($C_0 = 70 \pm 1$ ppmv). C_t and $C_{t\text{CO}_2}$ are the concentrations of VOCs and

formed CO₂ at a certain reaction time, respectively. N is the number of carbon atoms in VOCs.

Dark adsorption and photocatalytic oxidation of typical VOCs. The dark adsorption and photocatalytic tests were performed under the same reaction conditions as that described above, except that the dark adsorption equilibrium of VOCs on the catalysts will be taken into account prior to photocatalytic oxidation.

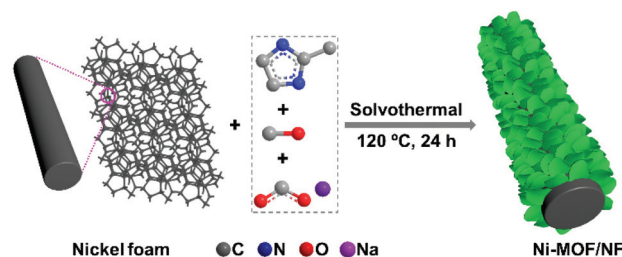
Ethyl acetate was chosen as a model VOC to investigate the dependence of the photocatalytic activity and generated intermediates on different flow rates of VOC gas. These tests were performed under the same reaction conditions as those for the dark adsorption and photocatalytic oxidation, except that the flow rates of VOC gas were varied from 10 to 60 mL min⁻¹. Moreover, a Proton Transfer Reaction Time-of-Flight Mass Spectrometer (PTR-ToF-MS, Ionicon Analytik GmbH, Austria) was employed for online monitoring and identification of the generated intermediates during the photocatalytic degradation process.

Evaluation of reactive species. The produced $\cdot\text{O}^{2-}$ and $\cdot\text{OH}$ radicals were detected using an electron paramagnetic resonance (EPR) spectrometer (EMXPlus-10/12, Bruker). DMPO was employed as the trapping agent and a 300 W Xenon lamp was used as the light source.

3. Results and discussion

3.1. Material characterization

As illustrated in Scheme 1, the vertically aligned Ni-MOF nanosheets on porous Ni foam were directly prepared *via* a simple solvothermal process. In this process, Ni foam not only served as the support for vertical growth of Ni-MOF nanosheets to alleviate random and lateral stacking between MOF nanosheets, but also acted as a self-sacrificial template to afford Ni ions for MOF growth assisted by the oxidation of air and water. Then, the surface morphology and composition of the synthesized samples were observed by SEM. As shown in Fig. 1a and b, the Ni foam possessed macroporosity and a smooth surface. The powder Ni-MOF exhibited a sphere with various sizes ranging from nanometers to micrometers composed of agglomerated nanosheets (Fig. S3†). In contrast, it could be clearly observed that plenty of nanosheets vertically and uniformly grew on the Ni foam surface and the agglomera-



Scheme 1 Illustration of the *in situ* preparation of Ni-MOF/NF.

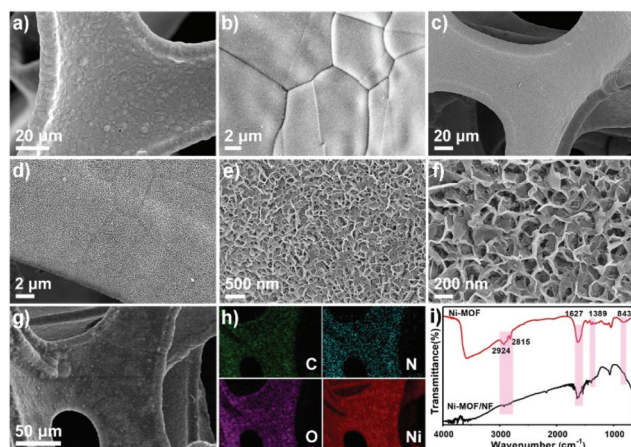


Fig. 1 SEM images of the activated Ni foam (a, b). SEM images of Ni-MOF/NF at different resolutions (c–g) and the corresponding elemental mapping images (h). FT-IR spectra of Ni-MOF and Ni-MOF/NF (i).

tion of nanosheets was effectively inhibited (Fig. 1c–f). The spacing between adjacent sheet layers was approximately tens of nanometres, which is conducive to light penetration, rapid mass transport and electron transfer.²⁶ The Energy Dispersive Spectrometry (EDS) mappings distinctly reflected the existence of C, N, O and Ni elements and homogeneously distributed on the sheet surface (Fig. 1g and h), implying that the nanosheets grew on Ni foam probably were Ni-MOF.

To further verify the structure of nanosheets, Fourier transform infrared spectroscopy (FT-IR) measurements were also performed. The FT-IR spectrum of powder Ni-MOF in Fig. 1i showed the characteristic absorption peaks located at 2924 and 2815 cm^{-1} , which were attributed to the C–H stretching vibration of the imidazole ring according to ref. 31 and 32. The band at 1627 cm^{-1} could be assigned to the C=N stretching vibration.³³ The peaks in the region of 843 from 1389 cm^{-1} would be ascribed to the imidazole ring bending and stretching.^{31–33} Remarkably, the characteristic peaks of Ni-MOF/NF well inherited that of the Ni-MOF (Fig. 1i and S4†), suggesting that the nanosheets covered on the Ni foam were the same as those on Ni-MOF. Additionally, the N_2 adsorption-desorption isotherms of powder Ni-MOF in Fig. S5† showed a typical type IV curve with a hysteresis loop due to the presence of mesopores. The calculated BET specific surface area and total pore volume of Ni-MOF based on the isotherms are listed in Table S1† as 22.07 $\text{m}^2 \text{g}^{-1}$ and 0.058 $\text{cm}^3 \text{g}^{-1}$, respectively. The Ni-MOF nanosheets were lacking bulk porosity for gas adsorption which is probably relevant to their extremely low specific surface area and pore volume.³⁴

The thermal resistance of powder Ni-MOF and Ni-MOF/NF was also investigated through thermogravimetric analysis (TGA) under a N_2 atmosphere. As indicated in Fig. S6a,† a slight weight loss appeared below 100 °C because of the evaporation of water adsorbed on the powder Ni-MOF. Subsequently, the powder Ni-MOF underwent an obvious weight loss between 300 °C and 500 °C probably due to the collapse of the MOF skeleton. Due to the extremely high thermal

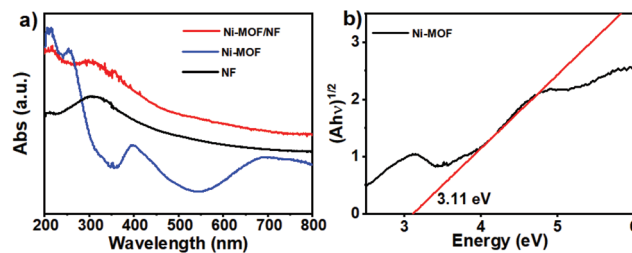


Fig. 2 UV-Vis diffuse reflectance spectra of the NF, powder Ni-MOF and Ni-MOF/NF (a) and the Tauc plot of Ni-MOF (b).

stability of Ni foam, the weight loss of the Ni-MOF/NF sample in the range of 200 °C–400 °C could be attributed to the decomposition of Ni-MOF nanosheets (Fig. S6b†). Distinctly, the decomposition temperature of Ni-MOF nanosheets in the Ni-MOF/NF sample was lower than that of powder Ni-MOF. This could be related to the low content and high dispersion of Ni-MOF nanosheets on the Ni foam surface which facilitate a rapid decomposition of Ni-MOF. Considering that the structure of Ni-MOF nanosheets in the Ni-MOF/NF sample was identical to that of powder Ni-MOF, the weight losses caused by the decomposition of Ni-MOF in both powder Ni-MOF and Ni-MOF/NF should be essentially the same. Thus, the loading of Ni-MOF nanosheets in the Ni-MOF/NF sample was approximately 0.57 wt% estimated using the following equation:

$$\text{The Ni-MOF nanosheet loading} = \frac{m_1 \times (m_3 - m_4)}{m_3 \times (m_1 - m_2)}$$

where m_1 is the weight of dry powder Ni-MOF, m_2 is the weight of the residues after the Ni-MOF decomposition, m_3 is the weight of the dry Ni-MOF/NF sample, and m_4 is the weight of the residues after the Ni-MOF/NF decomposition (Fig. S6†).

To further obtain the optical response of Ni-MOF, NF and Ni-MOF/NF, UV-vis diffuse reflectance measurements were also performed. As observed in Fig. 2, the Ni foam showed a weak absorption peak at ca. 330 nm. With regard to the pure Ni-MOF, three absorption peaks in the region of around 200–250, 350–500, and 600–800 nm were observed, indicating that it could harvest solar light. Notably, Ni-MOF/NF has a remarkably higher light absorption intensity than those of pure Ni-MOF and Ni foam, despite the very low loading of Ni-MOF in Ni foam. This phenomenon could be relevant to the special structure of Ni-MOF/NF in which macroporous Ni foam and well-aligned Ni-MOF nanosheets with a size of tens of nanometers could promote light penetration and allow the photoresponsive units to highly expose to solar light, thus enhancing the light harvesting. Additionally, the band gap of the Ni-MOF estimated from the Tauc plots was 3.11 V (Fig. 2b).

3.2. Photocatalytic performance evaluation

Paints are extensively applied in the furniture industry, building work, the automobile industry and the painting industry. However, various VOCs would inevitably release into the atmosphere during the spraying process and lead to serious threats to both humans and ecosystems. Thus, we chose three typical

groups of VOCs, including oxygenated VOCs (ethyl acetate), aliphatic VOCs (*n*-butanol) and aromatic VOCs (toluene), emitted from the industrial spraying process as model substrates to evaluate the adsorption and photocatalytic oxidation performance onto Ni-MOF/NF under visible light irradiation. The adsorption and degradation experiments were performed under 70 ppmv VOCs balanced in dry air with a flow rate of 35 mL min⁻¹. To verify the stability of Ni-MOF/NF under the investigated photocatalytic conditions, a photocatalytic trial was performed by illuminating the Ni-MOF/NF alone for 6 h under continuous dry air without VOCs at a flow rate of 35 mL min⁻¹ (Fig. S7†). The results showed that no CO₂ was generated, indicating that Ni-MOF/NF was stable under the photocatalytic conditions.

Initially, ethyl acetate was chosen as the model substrate to evaluate the photocatalytic performance of Ni-MOF/NF. As Fig. 3a shows, ethyl acetate quickly disappeared within 40 min and the removal efficiencies subsequently remained at around 89.7% within 360 min of illumination accompanied by the produced CO₂ of 113.7 ppmv. Based on the stoichiometric ratio between ethyl acetate and CO₂, it could be estimated that approximately 40.6% of ethyl acetate was mineralized into CO₂ (Fig. 3b), implying that the main degradation process by the Ni-MOF/NF photocatalyst was the mineralization of ethyl acetate to CO₂. For comparison, the photocatalytic oxidation of ethyl acetate was also performed using Degussa P25 as the catalyst (Fig. 3). It could be observed that the removal efficiency of ethyl acetate by Degussa P25 reached the maximum of 93.3% within 100 min accompanied by a mineralization efficiency of 8.6%, and then gradually decreased. Moreover, the color of Degussa P25 turned from white to light yellow within 360 min of illumination. These results suggested that Ni-MOF/NF exhibited higher photocatalytic performance and stability than commercial Degussa P25.

The scope of the photocatalytic system was subsequently applied in the oxidation of aliphatic *n*-butanol and aromatic toluene. The results depicted in Fig. 3 proved that the presented catalytic system was also amenable to the degradation of aliphatic and aromatic VOCs. The removal and mineralization efficiencies of *n*-butanol on the Ni-MOF/NF were 89.7% and 37.3% within 360 min of illumination, respectively, which were similar to those of ethyl acetate. Nevertheless, the Ni-MOF/NF showed only 19.9% of removal efficiency and 15.9%

of mineralization efficiency of toluene, which is distinctly lower than those of ethyl acetate and *n*-butanol. Remarkably, the selectivity to CO₂ formation during the degradation of ethyl acetate and *n*-butanol was 45.3% and 41.6%, which had no obvious differences. But the selectivity of toluene to CO₂ was 79.9%, which was significantly higher than that of the other two. Considering that the adsorption of VOCs on the photocatalyst surface plays a crucial role in the photocatalytic performance,¹⁰ the distinct activity differences among the three VOCs might be relevant to their adsorption capacities on Ni-MOF/NF.

Thus, adsorption experiments were also carried out under dark conditions prior to light irradiation to evaluate the effects of the VOC adsorption capability onto the Ni-MOF/NF on the photocatalytic oxidation. Initially, the reactions in the absence of a catalyst or using the activated Ni foam gave no adsorption amounts within 120 min. Comparatively, ethyl acetate in outlet gas quickly decreased to 42.7% within 5 min in the presence of Ni-MOF/NF, and subsequently began to increase and reached adsorption equilibrium within 50 min (Fig. 4a). For comparison, we also investigated the adsorption performance of ethyl acetate on the powder Ni-MOF. The results showed that 47.6% of ethyl acetate was absorbed on the surface of powder Ni-MOF within 10 min and reached adsorption equilibrium within 80 min (Fig. S8†), which exhibited a slightly higher adsorption amount than Ni-MOF/NF. For *n*-butanol, similar adsorption kinetic curves with ethyl acetate were observed, and the time for the lowest concentration of 41.1% and complete breakthrough was achieved as 5 and 15 min, respectively (Fig. S9†). However, when toluene was introduced, only 14.8% of toluene was absorbed within the initial 5 min, and then complete breakthrough was quickly achieved within 15 min (Fig. S10†).

After the adsorption equilibrium was achieved, the lamp was turned on and the photocatalytic reaction began. The results demonstrated that <1% of ethyl acetate, *n*-butanol and toluene were degraded within 200 min illumination in the absence of a catalyst or using the activated Ni foam, (Fig. 4b, c, S9 and S10†), suggesting that the effect of direct photolysis and Ni foam could be ignorable under the investigated conditions. When the Ni-MOF/NF was used as the photocatalyst, the removal efficiencies of ethyl acetate, *n*-butanol and toluene

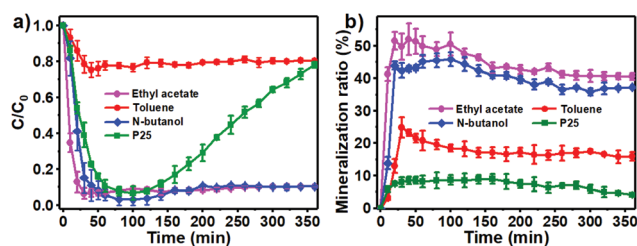


Fig. 3 Removal efficiency (a) and mineralization efficiency (b) of ethyl acetate, toluene and *n*-butanol during the direct photocatalytic oxidation using Ni-MOF/NF and Degussa P25.

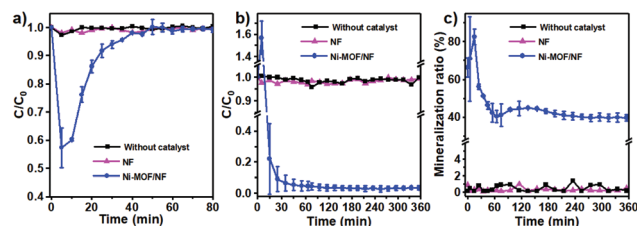


Fig. 4 Adsorption kinetic curves of ethyl acetate by the Ni-MOF/NF, Ni foam and without a photocatalyst (a). Removal efficiency (b) and mineralization efficiency (c) of ethyl acetate during the photocatalytic oxidation by the Ni-MOF/NF, Ni foam and a sample without a photocatalyst.

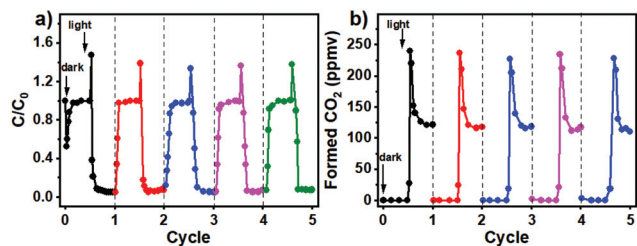


Fig. 5 Adsorption kinetic curves and removal efficiencies (a) as well as formed CO_2 (b) during the adsorption-photocatalytic oxidation cycles of ethyl acetate by Ni-MOF/NF.

rapidly reached 96.7%, 97.6% and 25.4% within 35 min, accompanied by the mineralization efficiencies of 39.9%, 39.7% and 24.0%, respectively. Note that the evolution curves of the formed CO_2 during oxidation of the three different VOCs all rapidly rose and then dropped to the stable level. This phenomenon could be relevant to their high VOC pre-adsorption amounts on Ni-MOF/NF. During the dark adsorption, more VOCs pre-adsorbed on the surface of Ni-MOF/NF would prolong the contact time between VOCs and photocatalytic active sites for the degradation compared with that in the direct photocatalytic oxidation, thus exhibiting high CO_2 formation. As the pre-adsorbed VOCs were consumed, the CO_2 amount gradually declined and then stabilized. The above results suggested that pre-capture of VOCs could greatly affect the photocatalytic activity. Moreover, the Ni-MOF/NF exhibited lower removal efficiency in the direct photocatalytic oxidation of toluene than those of both ethyl acetate and *n*-butanol, which might be correlated with the lower toluene adsorption capability of Ni-MOF/NF.

Furthermore, the reusability of Ni-MOF/NF was investigated by the photocatalytic oxidation of ethyl acetate. No appreciable changes in photocatalytic activity and CO_2 production were observed even after five recycle runs (Fig. 5), suggesting that the Ni-MOF/NF was stable under the investigated photocatalytic conditions.

3.3. Photocatalytic reaction mechanism

To investigate the dramatic activity differences between powder Ni-MOF and Ni-MOF/NF, photocurrent response tests based on variable voltage linear sweep voltammograms (LSVs) and the constant voltage amperometric method were firstly performed to investigate the charge transfer and the recombination behaviour of the photoexcited carriers in the photocatalysts (Fig. 6a, b and S11†). Fig. 6a and S11† show the LSV curves of Ni-MOF, Ni foam and Ni-MOF/NF under different light illumination conditions. Hardly any photocurrent of the Ni-MOF/NF was observed under darkness. After illuminating with visible light, the photocurrent of Ni-MOF/NF enhanced significantly with the increase of voltage in the range of 1.0–1.5 V regardless of constant light illumination and light on/off cycles. Moreover, the photocurrent of Ni-MOF/NF was much higher than those of both Ni-MOF and Ni foam under the same light illumination conditions. Furthermore, the tran-

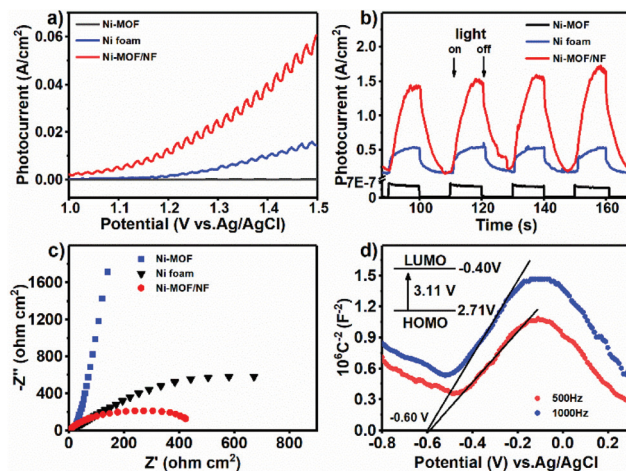


Fig. 6 Photocurrent responses tested using the linear sweep voltammetry curve (a) and a constant voltage amperometric method under intermittent irradiation (b) of the Ni-MOF/NF, Ni foam and Ni-MOF. EIS Nyquist plots of the Ni-MOF/NF, Ni foam and Ni-MOF (c). Mott-Schottky plots for Ni-MOF/NF at frequencies of 500 and 1000 Hz (d).

sient photocurrent responses of three catalysts were also investigated comparably *via* on-off cycles under intermittent light illumination. As Fig. 6b shows, the photocurrent of the powder Ni-MOF, Ni foam and Ni-MOF/NF instantly increased to a constant value after turning on the light and rapidly decreased to near zero after turning off the light, revealing an excellent reproducibility of the tests. For powder Ni-MOF, a negligible photocurrent signal emerged after turning on the light. When the Ni-MOF nanosheets grew on Ni foam, the photocurrent remarkably increased as compared with both powder Ni-MOF and Ni foam. Particularly, the stable photocurrent value of Ni-MOF/NF under light illumination was approximately 7 orders of magnitude higher than that of Ni-MOF. This indicated that Ni-MOF nanosheets grown vertically well-aligned on Ni foam could effectively accelerate the interfacial charge transfer and fast separation of photogenerated e^-h^+ , which have a vital impact on their photocatalytic activities.

To gain deep insight into the effect of the charge transfer behaviours of Ni-MOF, Ni foam and Ni-MOF/NF, the electrochemical evaluation was also performed using EIS. Only one semicircle or arc was observed in their Nyquist plots (Fig. 6c and S12†), indicating that the photocatalytic process involves the charge transfer-limit and the electron transfer rate would determine the recombination rate of photoexcited carriers.^{35,36} The powder Ni-MOF had the largest resistance radius. Strikingly, the resistance radius of Ni-MOF/NF was significantly shortened, implying that Ni-MOF/NF possesses the highest ability of electron transfer. Moreover, the charge transfer resistance of Ni-MOF and Ni-MOF/NF was 467.03 and 0.59 kΩ, respectively (Table S2†). This would be related to the conductivity of the Ni foam and the highly vertically oriented structure which was conducive to shortening electron transfer paths and accelerating electron transfer.^{26,27} Thus, the significant differences in electron transfer and the separation

efficiency of photogenerated carriers between Ni-MOF and Ni-MOF/NF would give rise to their different photocatalytic performance.

The band structures of Ni-MOF and Ni-MOF/NF were measured using typical Mott–Schottky plots to evaluate their oxidizing ability. The positive slopes of the C^{-2} to the potential plots (Fig. 6d and S13†) indicated the typical n-type semiconductor characteristics of powder Ni-MOF and Ni-MOF/NF. Additionally, the flat band positions of powder Ni-MOF and Ni-MOF/NF derived from their corresponding Mott–Schottky plots were approximately -0.90 and -0.60 V vs. Ag/AgCl, respectively. Accordingly, the conduction band (CB) of powder Ni-MOF and Ni-MOF/NF was calculated to be -0.70 and -0.40 V vs. NHE, respectively, which were both more negative than the $O_2/O_2^{\cdot-}$ potential (-0.33 V).³⁷ Thus, it was reasonably expected that both the Ni-MOF and Ni-MOF/NF have the potential to generate $\cdot O_2^{\cdot-}$ on their surface under light irradiation by reacting photogenerated e^- with surface adsorbed O_2 . Combined with their band gap energy obtained by Tauc plots (Fig. 2), the valence band (VB) potentials of Ni-MOF and Ni-MOF/NF were also estimated to be 2.41 and 2.71 V vs. NHE, respectively.

EPR experiments using DMPO as the spin trapping reagent were further carried out to examine the potential reactive oxygen species during the photocatalytic oxidation by Ni-MOF/NF (Fig. 7). There were no signals of both $\cdot O_2^{\cdot-}$ and $\cdot OH$ without light illumination. When the light was turned on, distinct characteristic sextet peaks belonging to the DMPO- $\cdot O_2^{\cdot-}$ adduct appeared and drastically increased with the prolonging illumination time, implying that the Ni-MOF/NF was really capable of producing $\cdot O_2^{\cdot-}$ radicals during the photocatalytic oxidation. It is well accepted that the adsorbed O_2 on the surface of the catalyst receives photogenerated e^- to produce $\cdot O_2^{\cdot-}$ radicals.^{38,39} As demonstrated by the SEM and photoelectrochemical results, the Ni-MOF nanosheets grown vertically well-aligned on Ni foam and the porous Ni foam had excellent electron conductivity, which are beneficial for the transfer of photogenerated e^- to highly accessible O_2 adsorption sites to form $\cdot O_2^{\cdot-}$ radicals. Moreover, abundant $\cdot OH$ radicals were sharply generated under visible light illumination and no apparent increase was found with the prolonging irradiation time, indicating the rapid formation of $\cdot OH$ radicals. However,

almost no $\cdot O_2^{\cdot-}$ and $\cdot OH$ radicals were formed over the powder Ni-MOF after 10 min of light illumination under the same conditions as Ni-MOF/NF (Fig. 7).

In the flowing gaseous heterogeneous photocatalytic system, the residence time of intermediates and reactants on active sites would be very important for the photocatalytic activity.^{10,40,41} Consequently, the photocatalytic reactions of ethyl acetate over Ni-MOF/NF were performed at flow rates ranging from 10 to 60 mL min^{-1} and the intermediates were monitored using PTR-ToF-MS. It could be found that the adsorbed amount of ethyl acetate by Ni-MOF/NF was gradually improved with decreasing flow rates in the dark adsorption experiments (Fig. S14a†). After the light was turned on, similar roll-up evolution curves of ethyl acetate and formed CO_2 were observed regardless of the different flow rates, and the concentrations of ethyl acetate and formed CO_2 instantly increased and subsequently declined to a constant level. Notably, the removal efficiency of ethyl acetate, formed CO_2 amount and CO_2 selectivity also increased significantly as the flow rates decreased (Fig. S14 and Table S3†). Particularly, the CO_2 selectivity reached 88.3% at 98.1% of ethyl acetate removal efficiency at a flow rate of 10 mL min^{-1} , but there were only 19.2% of CO_2 selectivity at 57.7% of ethyl acetate removal efficiency with a flow rate of 60 mL min^{-1} after 360 min illumination. The above results suggested that the adsorption and photocatalytic oxidation performance of ethyl acetate by Ni-MOF/NF were significantly related to its residence time on Ni-MOF/NF.

To further clarify the possible reaction mechanisms, PTR-ToF-MS was employed to identify and quantify the intermediates during the photocatalytic oxidation of ethyl acetate. Regardless of the different flow rates, the detected main intermediates showed almost no obvious difference which included formaldehyde, acetaldehyde, formic acid, alcohol, acetic acid and acetone (Fig. 8, Fig. S15 and Table S4†), indicating that the involved reaction pathways would not be altered by the flow rates. However, the contents of each intermediate at various flow rates were different distinctly. Interestingly, the contents of formaldehyde, alcohol and acetone all increased with the decrease in flow rate and clearly lower than the other three intermediates, but with regard to formic acid, acetaldehyde and acetic acid, their formations were all improved as the flow rates increased.

Considering that the dissociation energies of the C–C, C–O, C–H and C=O bonds were 3.44 , 3.38 , 4.29 and 7.55 eV, respectively,^{42,43} it would be deduced that ethyl acetate was attacked by the formed $\cdot O_2^{\cdot-}$, $\cdot OH$ and h^+ , and likely initially broke down into $CH_3CH_2\cdot$, $CH_3COO\cdot$, $CH_3CH_2O\cdot$, $CH_3CO\cdot$, $CH_3\cdot$ and $COO\cdot$ via the rupture of C–O and C–C bonds.^{44,45} Upon consideration of the observed time profiles of the dominated intermediate distribution as well as the literature reports,^{44–48} the photocatalytic oxidation of ethyl acetate might involve three reaction routes (Scheme 2). Only a trace amount of alcohol was observed probably due to its strong adsorption on the Ni-MOF/NF, which is beneficial to be further oxidized to acetaldehyde, acetic acid and formic acid.^{48–50} However,

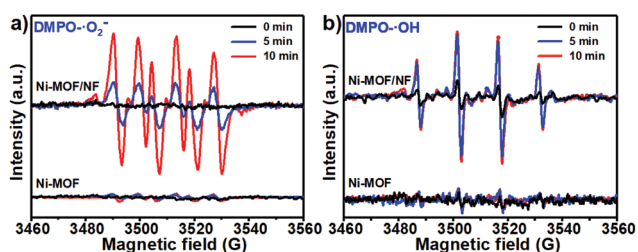


Fig. 7 DMPO spin-trapping EPR spectra recorded at ambient temperature in the presence of Ni-MOF/NF at $t = 0, 5$, and 10 min for DMPO- $\cdot O_2^{\cdot-}$ formed in irradiated methanol dispersion (a), and DMPO- $\cdot OH$ formed in irradiated H_2O dispersion (b).

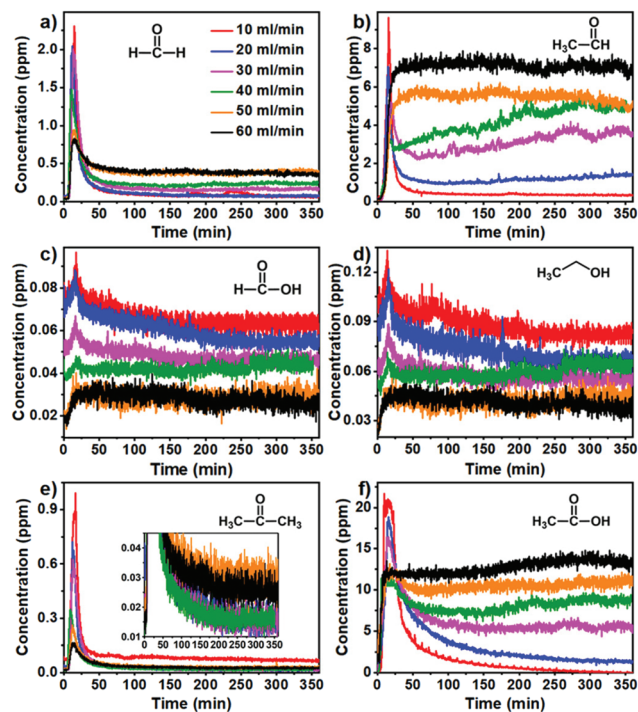
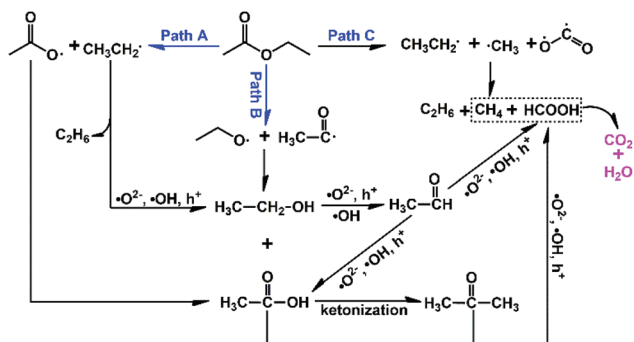


Fig. 8 Evolution of the produced intermediates during the photocatalytic oxidation of ethyl acetate by Ni-MOF/NF at different flow rates. The inset in (e) shows the enlarged (e) with a vertical axis in the range of 0.01–0.045 ppm.



Scheme 2 Possible reaction pathways for the photocatalytic oxidation of ethyl acetate.

acetone was appeared in a very small amount and declined with an increase in flow rate within 50 min, and then the amounts of acetone were almost the same at different flow rates ranging from 20 to 60 mL min⁻¹, indicating that acetone as a minor intermediate possibly resulted from the ketonization of acetic acid.⁴⁶

4. Conclusions

In summary, well-aligned Ni-MOF nanosheet arrays have been successfully grown on porous Ni foam by a facile *in situ* solvo-

thermal strategy using Ni foam as both a self-sacrificing template to offer Ni ions for MOF assembly and a substrate for vertical growth of Ni-MOF nanosheets. Remarkably, the Ni-MOF/Ni nanosheet arrays exhibited excellent photocatalytic activities and mineralization capability as well as high stability in the visible light driven photocatalytic oxidation of typical gaseous VOCs, which can be attributed to their unique architecture. In such a configuration, macroporous Ni foam and Ni-MOF nanosheet arrays afforded negligible diffusion limitations and boosted light harvesting due to convenient light penetration. Moreover, the excellent conductivity of Ni foam and well-aligned Ni-MOF nanosheets could offer fast mass and e⁻ transport channels, thus benefitting the separation of photogenerated e⁻-h⁺ pairs. Under the above synergistic effects, the Ni-MOF/Ni could produce abundant strong oxidative species, such as ·O²⁻ and ·OH radicals as well as photogenerated h⁺. Meanwhile, the effective capture and rapid diffusion of both VOCs and reaction intermediates could extend their residence time on the surface of Ni-MOF/NF, thus conducting the degradation of VOCs to CO₂ and H₂O by the strong oxidative species. This work demonstrates that the 2D MOF nanosheet arrays grown on the macroporous conductive Ni foam substrate would provide new opportunities for the development of superior photocatalysts.

Conflicts of interest

There are no conflicts to declare.

Acknowledgements

This work was supported by the National Natural Science Foundation of China (41425015 and 41731279), the Local Innovative and Research Teams Project of Guangdong Pearl River Talents Program (2017BT01Z032), the Pearl River S&T Nova Program of Guangzhou (201806010177), the Guangdong Special Support Plan for Science and Technology for Innovation Leading Scientists (2016TX03Z094 and 2016TQ03Z291) and the Natural Science Foundation of Guangdong (2019A1515010989).

References

- C. He, J. Cheng, X. Zhang, M. Douthwaite, S. Patisson and Z. Hao, *Chem. Rev.*, 2019, **119**, 4471–4568.
- M. Hakim, Y. Y. Broza, O. Barash, N. Peled, M. Phillips, A. Amann and H. Haick, *Chem. Rev.*, 2012, **112**, 5949–5966.
- A. Mellouki, T. J. Wallington and J. Chen, *Chem. Rev.*, 2015, **115**, 3984–4014.
- Y. Ji, J. Zhao, H. Terazono, K. Misawa, N. P. Levitt, Y. Li, Y. Lin, J. Peng, Y. Wang, L. Duan, B. Pan, F. Zhang, X. Feng, T. An, W. Marrero-Ortiz, J. Secrest, A. L. Zhang, K. Shibuya, M. J. Molina and R. Zhang, *Proc. Natl. Acad. Sci. U. S. A.*, 2017, **114**, 8169–8174.

- 5 J. Kong, G. Li, M. Wen, J. Chen, H. Liu and T. An, *J. Catal.*, 2019, **370**, 88–96.
- 6 C. Yang, G. Miao, Y. Pi, Q. Xia, J. Wu, Z. Li and J. Xiao, *Chem. Eng. J.*, 2019, **370**, 1128–1153.
- 7 J. Chen, G. Li, Z. He and T. An, *J. Hazard. Mater.*, 2011, **190**, 416–423.
- 8 Y. Boyjoo, H. Sun, J. Liu, V. K. Pareek and S. Wang, *Chem. Eng. J.*, 2017, **310**, 537–559.
- 9 S. Weon and W. Choi, *Environ. Sci. Technol.*, 2016, **50**, 2556–2563.
- 10 A. H. Mamaghani, F. Haghghat and C. S. Lee, *Appl. Catal., B*, 2017, **203**, 247–269.
- 11 C. P. Xu, R. Q. Fang, R. Luque, L. Y. Chen and Y. W. Li, *Coord. Chem. Rev.*, 2019, **388**, 268–292.
- 12 X. Cui, W. Xu, Z. Xie and Y. Wang, *J. Mater. Chem. A*, 2016, **4**, 1908–1914.
- 13 W. Pang, B. Shao, X. Q. Tan, C. Tang, Z. Zhang and J. Huang, *Nanoscale*, 2020, **12**, 3623–3629.
- 14 M. Wen, G. Li, H. Liu, J. Chen, T. An and H. Yamashita, *Environ. Sci.: Nano*, 2019, **6**, 1006–1025.
- 15 N. S. Bobbitt, M. L. Mendonca, A. J. Howarth, T. Islamoglu, J. T. Hupp, O. K. Farha and R. Q. Snurr, *Chem. Soc. Rev.*, 2017, **46**, 3357–3385.
- 16 A. Liu, X. Peng, Q. Jin, S. K. Jain, J. M. Vicent-Luna, S. Calero and D. Zhao, *ACS Appl. Mater. Interfaces*, 2019, **11**, 4686–4700.
- 17 C. Xu, Y. Pan, G. Wan, H. Liu, L. Wang, H. Zhou, S. H. Yu and H. L. Jiang, *J. Am. Chem. Soc.*, 2019, **141**, 19110–19117.
- 18 A. Dhakshinamoorthy, Z. Li and H. Garcia, *Chem. Soc. Rev.*, 2018, **47**, 8134–8172.
- 19 X. He, H. Fang, D. J. Gosztola, Z. Jiang, P. Jena and W. N. Wang, *ACS Appl. Mater. Interfaces*, 2019, **11**, 12516–12524.
- 20 L. Chen, Y. Wang, F. Yu, X. Shen and C. Duan, *J. Mater. Chem. A*, 2019, **7**, 11355–11361.
- 21 Y. Wang, N. Y. Huang, J. Q. Shen, P. Q. Liao, X. M. Chen and J. P. Zhang, *J. Am. Chem. Soc.*, 2018, **140**, 38–41.
- 22 P. Yao, H. Liu, D. Wang, J. Chen, G. Li and T. An, *J. Colloid Interface Sci.*, 2018, **522**, 174–182.
- 23 Z. G. Zhang, X. Y. Li, B. J. Liu, Q. D. Zhao and G. H. Chen, *RSC Adv.*, 2016, **6**, 4289–4295.
- 24 J. Zhang, Y. Hu, J. Qin, Z. Yang and M. Fu, *Chem. Eng. J.*, 2020, **385**, 123814.
- 25 H. Liu, Y. Ma, J. Chen, M. Wen, G. Li and T. An, *Appl. Catal., B*, 2019, **250**, 337–346.
- 26 A. Dhakshinamoorthy, A. M. Asiri and H. Garcia, *Adv. Mater.*, 2019, **31**, e1900617.
- 27 Z. R. Tao, J. X. Wu, Y. J. Zhao, M. Xu, W. Q. Tang, Q. H. Zhang, L. Gu, D. H. Liu and Z. Y. Gu, *Nat. Commun.*, 2019, **10**, 2911.
- 28 S. Zhao, Y. Wang, J. Dong, C.-T. He, H. Yin, P. An, K. Zhao, X. Zhang, C. Gao, L. Zhang, J. Lv, J. Wang, J. Zhang, A. M. Khattak, N. A. Khan, Z. Wei, J. Zhang, S. Liu, H. Zhao and Z. Tang, *Nat. Energy*, 2016, **1**, 1–10.
- 29 F. Wu, X. Guo, G. Hao, Y. Hu and W. Jiang, *Nanoscale*, 2019, **11**, 14785–14792.
- 30 M. Zhang, G. Wang, B. Zheng, L. Li, B. Lv, H. Cao and M. Chen, *Nanoscale*, 2019, **11**, 5058–5063.
- 31 M. Zhang, Q. G. Shang, Y. Q. Wan, Q. R. Cheng, G. Y. Liao and Z. Q. Pan, *Appl. Catal., B*, 2019, **241**, 149–158.
- 32 N. M. Mahmoodi, M. Oveisi, A. Taghizadeh and M. Taghizadeh, *J. Hazard. Mater.*, 2019, **368**, 746–759.
- 33 A. Pongsombate, T. Imyen, P. Dittanet, B. Embley and P. Kongkachuichay, *J. Taiwan Inst. Chem. Eng.*, 2017, **80**, 16–24.
- 34 M. A. Solomos, F. J. Claire and T. J. Kempa, *J. Mater. Chem. A*, 2019, **7**, 23537–23562.
- 35 B. F. Xin, Z. Y. Ren, H. Y. Hu, X. Y. Zhang, C. L. Dong, K. Y. Shi, L. Q. Jing and H. G. Fu, *Appl. Surf. Sci.*, 2005, **252**, 2050–2055.
- 36 J. M. Kesselman, G. A. Shreve, M. R. Hoffmann and N. S. Lewis, *J. Phys. Chem.*, 1994, **98**, 13385–13395.
- 37 J. Li, X. A. Dong, G. Zhang, W. Cui, W. Cen, Z. Wu, S. C. Lee and F. Dong, *J. Mater. Chem. A*, 2019, **7**, 3366–3374.
- 38 Y. Nosaka and A. Y. Nosaka, *Chem. Rev.*, 2017, **117**, 11302–11336.
- 39 C. Chen, W. Ma and J. Zhao, *Chem. Soc. Rev.*, 2010, **39**, 4206–4219.
- 40 S. S. Lee, C. Y. Lu and M. C. Wu, *RSC Adv.*, 2018, **8**, 22199–22215.
- 41 K. Demeestere, J. Dewulf, B. De Witte and H. Van Langenhove, *Appl. Catal., B*, 2005, **60**, 93–106.
- 42 L. Magne, N. Blin-Simiand, K. Gadonna, P. Jeanney, F. Jorand, S. Pasquiers and C. Postel, *Eur. Phys. J.: Appl. Phys.*, 2009, **47**, 22816.
- 43 M. R. Nimlos, E. J. Wolfrum, M. L. Brewer, J. A. Fennell and G. Bintner, *Environ. Sci. Technol.*, 1996, **30**, 3102–3110.
- 44 D. Delimaris and T. Ioannides, *Appl. Catal., B*, 2009, **89**, 295–302.
- 45 H. Wang, S. Chen, Z. Wang, Y. Zhou and Z. Wu, *Appl. Catal., B*, 2019, **254**, 339–350.
- 46 T. K. Phung, M. M. Carnasciali, E. Finocchio and G. Busca, *Appl. Catal., A*, 2014, **470**, 72–80.
- 47 T. Tsoncheva, A. Mileva, G. Issa, M. Dimitrov, D. Kovacheva, J. Henych, M. Kormunda, N. Scotti, M. Slušná, J. Tolasz and V. Štengl, *J. Environ. Chem. Eng.*, 2018, **6**, 2540–2550.
- 48 T. Tsoncheva, A. Mileva, G. Issa, M. Dimitrov, D. Kovacheva, J. Henych, N. Scotti, M. Kormunda, G. Atanasova and V. Štengl, *Appl. Surf. Sci.*, 2017, **396**, 1289–1302.
- 49 V. Blasin-Aubé, J. Belkouch and L. Monceaux, *Appl. Catal., B*, 2003, **43**, 175–186.
- 50 C. Tang, X. Huang, H. Wang, H. Shi and G. Zhao, *J. Hazard. Mater.*, 2020, **382**, 121017–121025.